Supporting Information

Mazhab-Jafari et al. 10.1073/pnas.1419895112

SI Materials and Methods

Protein Preparation. A synthetic gene encoding human K-RAS4B (residues 1–185, bearing a single C118S mutation) was synthesized (Genscript) and ligated into pET-28 vector to express the protein with a thrombin-cleavable His-tag. The RAS-binding domains of human ARAF (ARAF-RBD, residues 17–94) and human RAL guanine dissociation stimulator (RALGDS, residues 741–833) were ligated into pGEX-4T2 to express a thrombin-cleavable GST fusion protein (1). The pGBHPS-MSP vector encoding membrane scaffold protein (MSP) variant 1D1 (2) was obtained through AddGene. Mutagenesis was carried out with a QuikChange Site-Directed Mutagenesis Kit (Agilent Technologies). Protein expression was performed as described previously (1, 3). In brief, K-RAS4B and RBDs of ARAF and RALGDS were expressed in *Escherichia coli* (BL21), either in Luria-Bertani (LB) broth or in minimal media supplemented with 1 mg/mL ^{15}N ammonium chloride and 70 mg/mL 2-keto-butyric acid-4-^{13}C to ^{13}C label the Cδ methyl groups of isoleucine residues (4). Expressions was induced with 0.25 mM isopropyl β-D-1-thiogalactopyranoside (IPTG) at 15 °C and an OD_{600} of 0.6 for 16 h. MSP1D1 was expressed in *E. coli* (BL21) grown in 2× yeast extract tryptone media in a LEX bioreactor system. Expression was induced at 37 °C with 1 mM IPTG at an OD_{600} of 2.5 for 1 h, followed by a 2.5-h incubation period at 28 °C. Following affinity purification (Ni-NTA or glutathione Sepharose) the His- or GST-tags were cleaved from K-RAS4B or ARAF and RALGDS RBDs, respectively, with thrombin, and the His-tag was cleaved from MSP1D1 with HRV3C protease. All proteins were further purified by size exclusion chromatography (Superdex 75; GE Healthcare). MSP1D1 was purified in nanodisc (ND) buffer (20 mM Tris, pH 7.4, 100 mM NaCl). K-RAS4B and the RBDs were purified in ND buffer containing 5 mM $MgCl_2$ and 2 mM tris(2-carboxyethyl)phosphine (TCEP).

Preparation of Nanodisc-Tethered K-RAS4B and RBD Complexes. Nanodiscs were prepared as previously described (3, 5) with a lipid composition of 1,2-dioleoyl-*sn*-glycero-3-phosphocholine (DOPC), 1,2-dioleoyl-*sn*-glycero-3-phospho-L-serine (DOPS), and the thiol-reactive lipid 1,2-dioleoyl-*sn*-glycero-3-phosphoethanolamine-*N*-[4-(p-maleimidomethyl)cyclohexane-carboxamide] (PE-MCC) in a molar ratio of 15:4:1 (Avanti Polar Lipids). For PRE experiments, this was supplemented with 1,2-distearoyl-*sn*-glycero-3-phosphoethanolamine-*N*-diethylenetriaminepentaacetic acid [gadolinium salt; PE-DTPA (Gd^{3+})] to a final molar ratio of 2.5% of the total lipids. PE-MCC in preassembled, purified nanodiscs was covalently linked to K-RAS4B as described previously (3). Nanodiscs containing K-RAS-GMPPNP were assembled by preloading K-RAS4B with GMPPNP in the presence of alkaline phosphatase and EDTA before nanodisc conjugation. The ARAF and RALGDS RBDs were added to nanodisc-tethered K-RAS4B at a molar ratio of 1.2:1, relative to K-RAS4B. Nanodisc-tethered K-RAS4B:RBD complexes were prepared with two isotopic labeling schemes: (*i*) Ile-^{13}Cδ–labeled K-RAS4B complexed with unlabeled RBD and (*ii*) Ile-^{13}Cδ–labeled RBD in complex with unlabeled K-RAS4B.

NMR Measurements. NMR measurements of nanodisc-bound samples were carried out on a Bruker AVANCE II 800-MHz spectrometer equipped with a 5-mm TCI CryoProbe, whereas a 600-MHz spectrometer equipped with a TCI 1.7-mm MicroCryoProbe was used to acquire spectra of nanodisc-free samples. All spectra were collected at a temperature of 298.2 K using samples containing 0.6 mM K-RAS4B. All NMR measurements were carried out in ND buffer containing 5 mM $MgCl_2$, 2 mM TCEP, pH 7.4, and 10% (vol/vol) D_2O. {^{1}H-^{13}C} HMQC spectra were collected with 8, 32, or 128 scans for isolated K-RAS4B, nanodisc-tethered K-RAS4B, and nanodisc-tethered K-RAS4B:ARAF-RBD complexes, respectively. The one-dimensional ^{31}P NMR spectra were collected with a Bruker AVANCE III 700-MHz spectrometer equipped with a 5-mm QNP-CryoProbe using a 30° pulse on isotopically unlabeled samples of K-RAS-GMPPNP WT and mutants of concentration 1.5–2.0 mM at temperatures of 278.2 and 298.2 K. The spectra were analyzed using previously reported phosphate resonance assignments (6). K-RAS4B isoleucine Cδ-methyl resonances were tentatively assigned based on assignments of H-RAS-GDP (kindly provided by Sharon Campbell, University of North Carolina, Chapel Hill, NC) and T35S H-RAS-GMPPNP [Biological Magnetic Resonance Bank (BMRB) code 17610], and remaining ambiguous assignments were resolved by mutagenesis of isoleucines 21, 36, 100, 139, and 163 to leucine residues. The ARAF-RBD isoleucine Cδ-methyl resonance assignments were transferred from BMRB entry 11265. NMR spectra were processed with NMRPipe (7) and analyzed with Sparky (https://www.cgl.ucsf.edu/home/sparky/). For PRE measurements, the resonance intensities of Ile-Cδ on PE-DTPA (Gd^{3+})–containing nanodiscs were compared with those of a control sample prepared without PE-DTPA (Gd^{3+}). The cross-peak intensities were measured using Sparky by Gaussian line fitting. The PRE and control samples were prepared at equal concentration based on their size exclusion chromatograms and SDS/PAGE. Any small difference in concentration was corrected by normalization of the calculated intensity ratios against the highest observed I^*/I^o (where I^* is the resonance intensities of Ile-Cδ on nanodiscs incorporating 2.5% Gd^{3+}-conjugated PE-DTPA, and I^o is that in the paramagnetic ion-free nanodiscs) for each GDP and GMPPNP plot. I84-Cδ, located near the nucleotide binding site, was least affected by PRE and was therefore used as the internal standard for normalization.

Derivation of K-RAS4B and Nanodisc Models. The structures of K-RAS4B (residues 1–185) were annealed in Crystallography & NMR System (CNS) (8) using the RECOORD scripts (9), with distance, hydrogen bond, and torsion angle restraints derived from the crystal structures of WT K-RAS4B GDP (PDB ID code 4LPK) and K-RAS4B Q61H GMPPNP (PDB ID code 3GFT). The active structure was back-mutated to Gln61 followed by energy minimization in CNS. The C-terminal helix was modeled using the crystallographic information from the structure of full-length K-RAS4B G12D (PDB ID code 4DSN). No restraints were given to the flexible C-terminal residues (174–185) during the simulated annealing protocol; thus, the K-RAS4B C terminus sampled large conformational variability in the final ensemble of structures. The starting nanodisc model for HADDOCK simulations were generated by inserting a model bilayer composed of 80 lipid molecules (80% DOPC, 20% DOPS), computed via CHARMM-GUI (10–12), into an MSP1D1 nanodisc model (13).

BLI Binding Assays. BLI assays of K-RAS4B–RBD interactions were performed using an Octet RED96 instrument (ForteBio). A fusion protein of GST and the RBD of ARAF (GST-ARAF-RBD) was immobilized on anti-GST antibody-coated biosensors in ND buffer containing 5 mM $MgCl_2$, 2 mM TCEP, 0.1 mg/mL BSA, and 0.002% Tween 20. A single batch of nanodiscs was prepared, from which equal aliquots were used for conjugation

to matched samples of WT and mutant K-RAS4B to ensure sample consistency. Total K-RAS4B–nanodisc complexes were monitored by absorbance at 280 nm, and the conjugation efficiency was assessed by detection of unconjugated K-RAS4B in size exclusion chromatography. The association of free and nanodisc-conjugated K-RAS4B WT, K5N, G12D, M67C, and D153V with the RBD was measured at a range of K-RAS4B concentrations (0, 0.35, 0.7, 3.5, 17.5, and 35 μM) for 400 s. The k_{OFF} rates were determined by transferring the biosensor to ND buffer for 700 s (Fig. 4 *C* and *D* and Fig. S7). Each k_{ON} and k_{OFF} rate was determined from data obtained using analyte concentrations of 0.7, 3.5, and 17.5 μM, and error bars represent the SD of three measurements of k_{ON} and k_{OFF} and propagated accordingly for the K_d values (Fig. 4 *C* and *D* and Fig. S7). The lowest (0.35 μM) and highest (35 μM) analyte concentrations were excluded because low signal amplitude or fast ON rates, respectively, reduced the measurement accuracy. K-RAS4B–nanodisc complexes did not completely dissociate during this washout step, likely due to aggregation on the biosensor; however, this effect was identical for WT K-RAS4B and each of the mutants. The nanodisc-tethered K-RAS4B complexes also exhibited weak (K_d = 3.5 μM) nonspecific binding to biosensors loaded with GST in the absence of A-RAFRBD, which was identical for WT and mutants; thus, this background was subtracted before curve fitting (Fig. S7 *C* and *D*). For these reasons, only relative k_{ON}, k_{OFF}, and K_d values for WT vs. mutants are reported.

1. Smith MJ, Ikura M (2014) Integrated RAS signaling defined by parallel NMR detection of effectors and regulators. *Nat Chem Biol* 10(3):223–230.
2. Ritchie TK, et al. (2009) Chapter 11: Reconstitution of membrane proteins in phospholipid bilayer nanodiscs. *Methods Enzymol* 464:211–231.
3. Mazhab-Jafari MT, et al. (2013) Membrane-dependent modulation of the mTOR activator Rheb: NMR observations of a GTPase tethered to a lipid-bilayer nanodisc. *J Am Chem Soc* 135(9):3367–3370.
4. Tugarinov V, Kanelis V, Kay LE (2006) Isotope labeling strategies for the study of high-molecular-weight proteins by solution NMR spectroscopy. *Nat Protoc* 1(2):749–754.
5. Kobashigawa Y, Harada K, Yoshida N, Ogura K, Inagaki F (2011) Phosphoinositide-incorporated lipid-protein nanodiscs: A tool for studying protein-lipid interactions. *Anal Biochem* 410(1):77–83.
6. Spoerner M, et al. (2005) Conformational states of Ras complexed with the GTP analogue GppNHp or GppCH2p: Implications for the interaction with effector proteins. *Biochemistry* 44(6):2225–2236.
7. Delaglio F, et al. (1995) NMRPipe: A multidimensional spectral processing system based on UNIX pipes. *J Biomol NMR* 6(3):277–293.
8. Brünger AT, et al. (1998) Crystallography & NMR system: A new software suite for macromolecular structure determination. *Acta Crystallogr D Biol Crystallogr* 54(Pt 5): 905–921.
9. Nederveen AJ, et al. (2005) RECOORD: A recalculated coordinate database of 500+ proteins from the PDB using restraints from the BioMagResBank. *Proteins* 59(4): 662–672.
10. Jo S, Lim JB, Klauda JB, Im W (2009) CHARMM-GUI Membrane Builder for mixed bilayers and its application to yeast membranes. *Biophys J* 97(1):50–58.
11. Jo S, Kim T, Iyer VG, Im W (2008) CHARMM-GUI: A web-based graphical user interface for CHARMM. *J Comput Chem* 29(11):1859–1865.
12. Jo S, Kim T, Im W (2007) Automated builder and database of protein/membrane complexes for molecular dynamics simulations. *PLoS ONE* 2(9):e880.
13. Segrest JP, et al. (1999) A detailed molecular belt model for apolipoprotein A-I in discoidal high density lipoprotein. *J Biol Chem* 274(45):31755–31758.

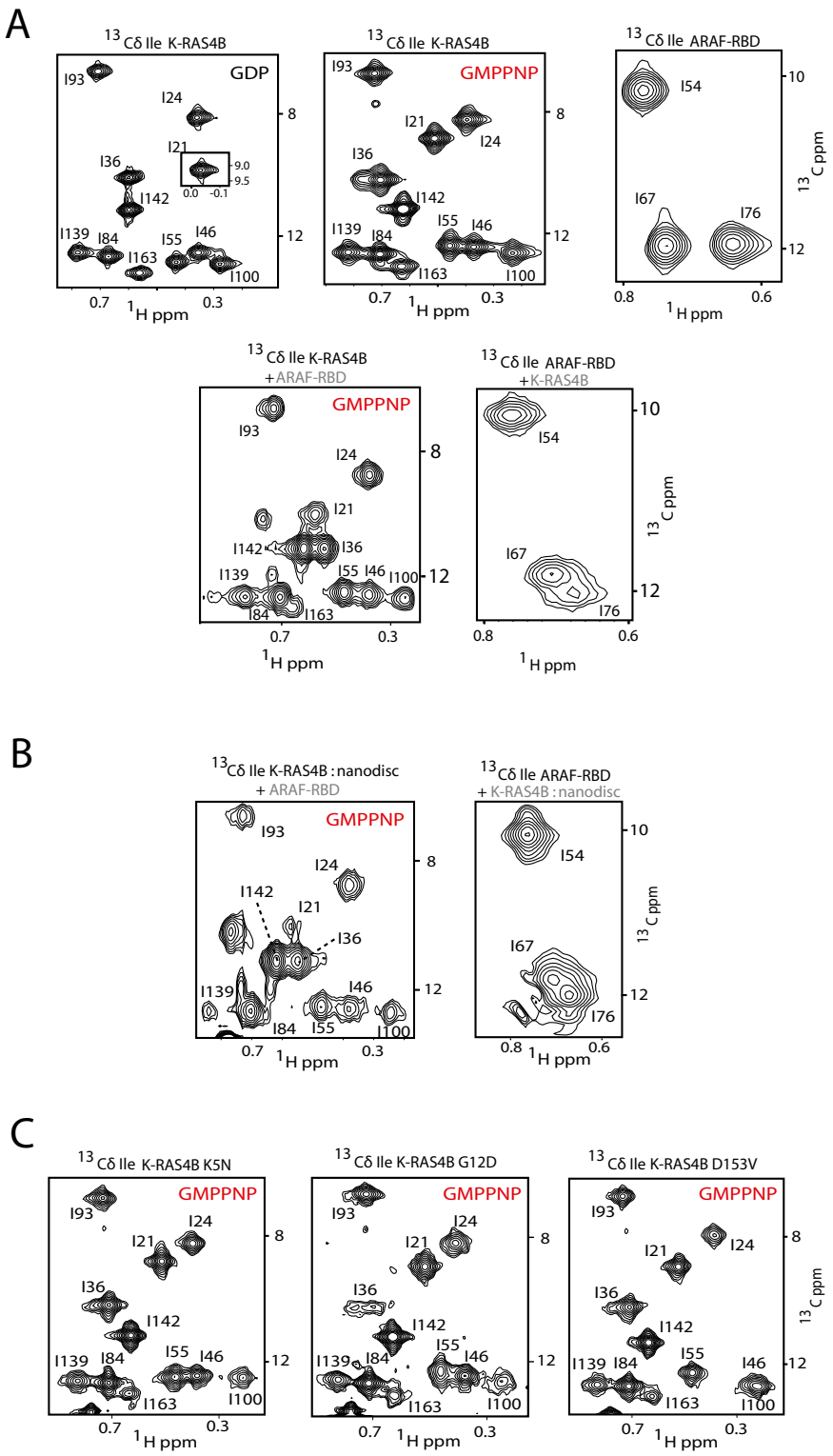

Fig. S1. ^{1}H-^{13}C HMQC spectra of WT and mutant K-RAS4B and its complexes with ARAF-RBD. (*A*) Spectra of ^{13}Cδ-Ile–labeled K-RAS4B and ARAF-RBD alone (*Upper*) and in complex (*Lower*) in the absence of nanodiscs. Isotopic labeling scheme is indicated above each spectrum. (*B*) Spectra of nanodisc-conjugated K-RAS:ARAF-RBD complexes labeled as indicated. (*C*) Spectra of disease associated K-RAS4B mutants (as indicated) tethered to nanodiscs.

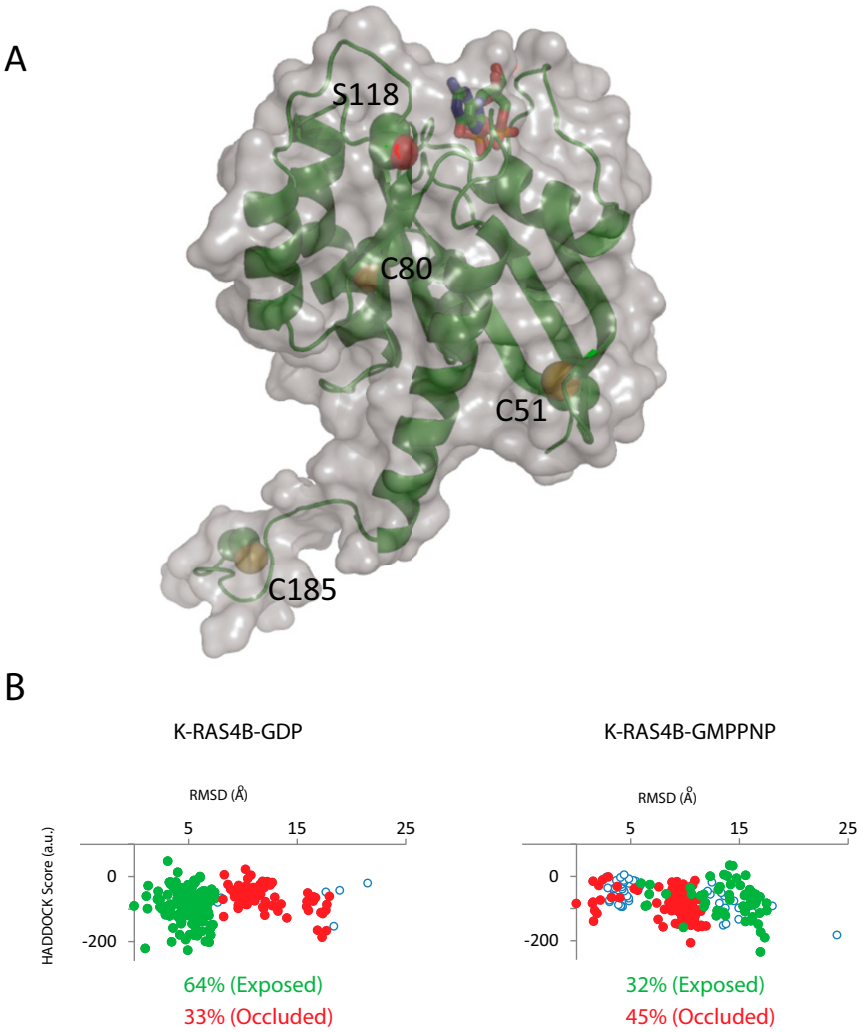

Fig. S2. K-RAS4B construct and cluster analysis of the final HADDOCK solutions. (*A*) K-RAS4B 1–185 was conjugated to a maleimide-functionalized lipid (PE-MCC) through the C-terminal CaaX-box residue Cys185. The surface exposed Cys118 was mutated to Ser to prevent reaction with the phospholipid. Cys51 and Cys80 are buried in the core of the protein and inaccessible to reaction with PE-MCC. (*B*) The final 200 K-RAS4B-nanodisc complex structures, represented on a plot of HADDOCK score vs. RMSD to the global mean structure (defined as the structure with lowest RMSD to all other 199 structures) for GDP- (*Left*) and GMPPNP-bound (*Right*) K-RAS4B-nanodisc simulations. Complex structures belonging to exposed and occluded clusters are highlighted in green and red, respectively, and relative populations are indicated.

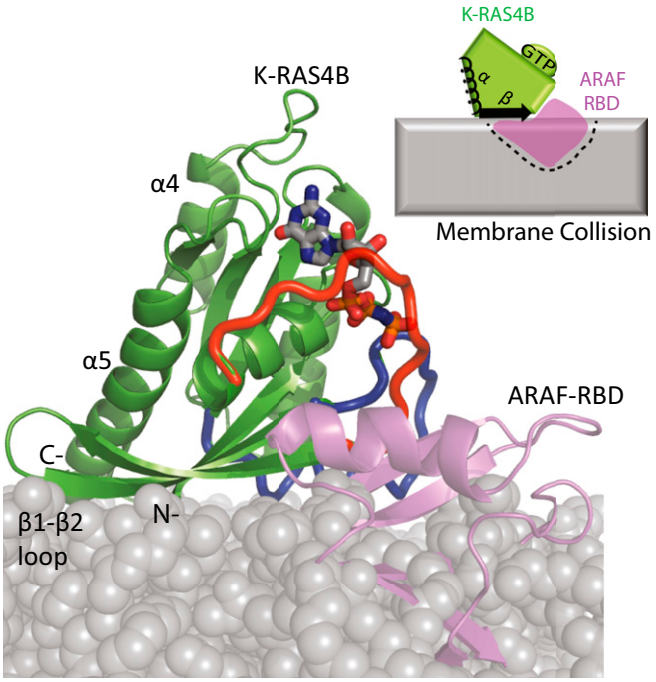

Fig. S3. Occluded orientation of membrane-tethered K-RAS4B is incompatible with RBD binding. The K-RAS4B:ARAF-RBD complex structure (model based on H-RAS:CRAF-RBD, PDB ID code 4G0N) aligned with the lowest scored HADDOCK-driven model of nanodisc-tethered K-RAS4B-GMPPNP alone. For simplicity, only one K-Ras molecule is shown. Note that in this orientation of K-RAS4B the RBD-binding site is blocked by steric clashes with the membrane, as illustrated by the dashed line in the inset schematic model.

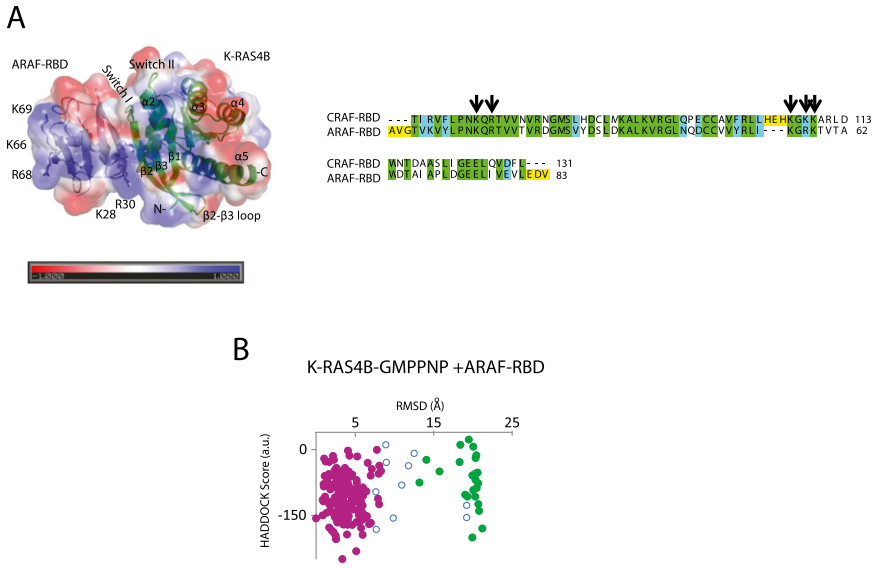

Fig. S4. Surface electrostatics of the K-RAS4B:ARAF-RBD complex and cluster analysis of the final HADDOCK solutions of the membrane-tethered complex. (*A*) Surface electrostatisc of the K-RAS4B:ARAF-RBD complex calculated as described in Fig. S2*B*. The predominant orientation is viewed from the membrane interface, and residues contributing to the positively charged patch on the RBD are indicated. (*Right*) Sequence alignment indicating conservation of the positively charged patch between the RBDs of ARAF and CRAF. (*B*) Cluster analysis of the final 200 refined models of HADDOCK simulation of K-RAS4B:ARAF-RBD-nanodisc complex. The predominant cluster (magenta) and the minor cluster (green) represent the semiexposed and exposed orientations, respectively.

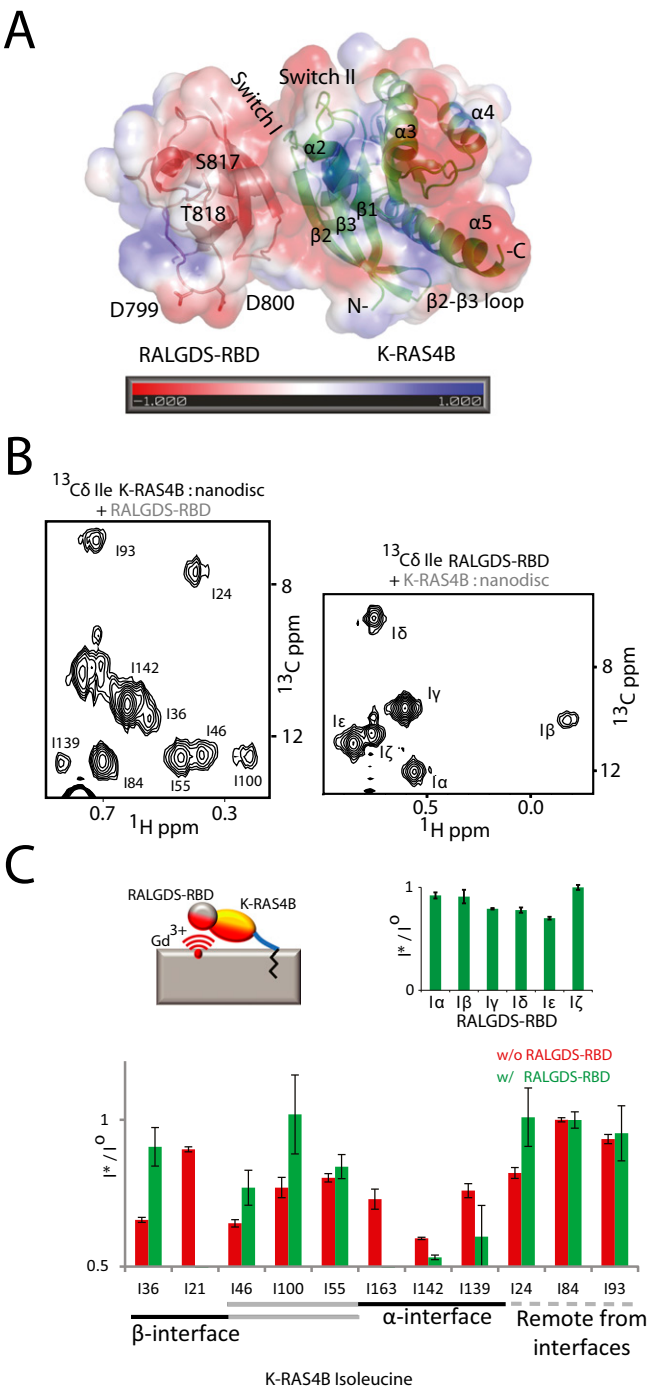

Fig. S5. K-RAS4B shifts toward an exposed orientation on binding the RBD of RALGDS. (*A*) Surface electrostatics of a complex of K-RAS4B with RBD of RALGDS (model based on PDB ID code 1LFD). The surface electrostatics were calculated as described in Fig. S2*B* and are viewed in the same orientation as K-RAS4B:ARAF-RBD in Fig. S4*A*. (*B*) ^{1}H-^{13}C HMQC spectra of nanodisc:K-RAS4B-GMPPNP:RALGDS-RBD complexes isotopically labeled as indicated. (*C*) Effect of RALGDS-RBD interaction with nanodisc-tethered K-RAS4B on PRE profiles. (*Upper*) PRE profile of RALGDS-RBD Ile-Cδ in the presence of Gd^{3+}-containing (I*) vs. Gd^{3+}-free (I^{o}) nanodisc-tethered K-RAS4B-GMPPNP. (*Lower*) Nanodisc-tethered K-RAS4B-GMPPNP, red; nanodisc-tethered K-RAS4B-GMPPNP:RALGDS-RBD complex, green (I* and I^{o} as above). Residues are grouped according to their location with respect to the α and β membrane interfaces. Error bars are based on spectral noise.

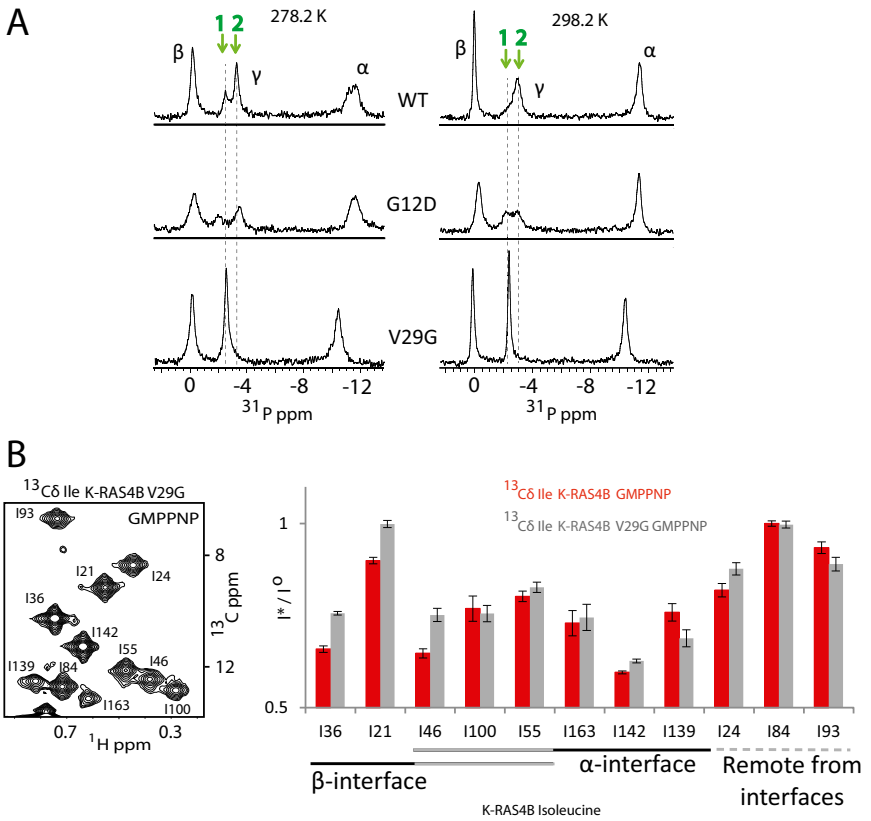

Fig. S6. Increase in the population of conformational state 1 shifts K-RAS4B toward the exposed orientation. (*A*) One-dimensional ^{31}P-NMR spectra of isolated WT K-RAS4B, the oncogenic mutant G12D, and the state 1-selective mutant V29G, all in complex with GMPPNP, at 278.2 (*Left*) and 298.2 K (*Right*). The chemical shift positions of the γ-phosphate resonances of state 1 and 2 are highlighted with dashed lines. (*B*) ^{1}H-^{13}C HMQC spectrum of nanodisc-conjugated ^{13}Cδ-Ile–labeled K-RAS4B V29G in complex with GMPPNP. (*Right*) Plot of PRE-induced broadening of K-RAS4B WT (red) vs. V29G (gray) resonances by Gd^{3+}-conjugated lipid incorporated into nanodiscs, as described in Fig. 2*A*. Residues are grouped according to their location with respect to the α and β membrane interfaces.

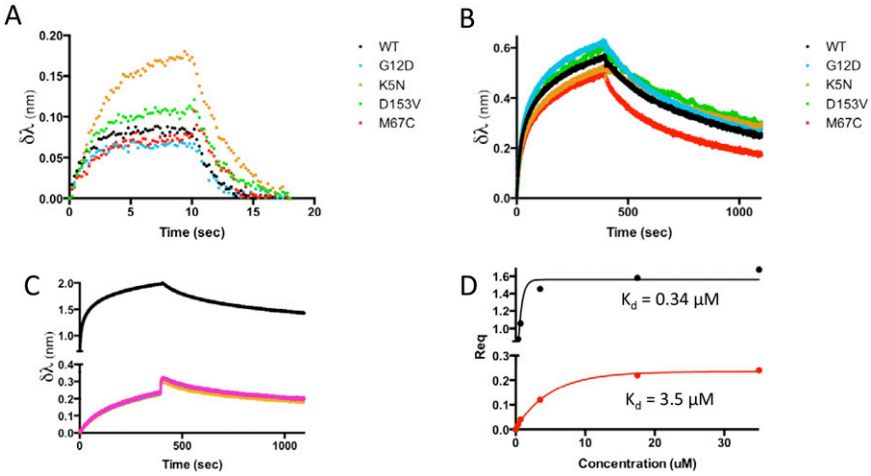

Fig. S7. Analyses of binding kinetics of free and nanodisc-tethered K-RAS4B and mutants. BLI (ForteBio Octet RED96) was used to directly measure the binding kinetics of K-RAS4B (analyte) to immobilized ARAF-RBD (ligand). (*A*) Binding curves for free WT K-RAS4B and mutants binding to GST-ARAF-RBD immobilized on an anti-GST biosensor. Relative association rates (k_{ON}), dissociation rates (k_{OFF}), and dissociation constants (K_d) for free K-RAS4B binding to ARAF-RBD are shown in Fig. 4*C*. (*B*) Binding curves for nanodisc-tethered WT K-RAS4B and mutants binding to GST-ARAF-RBD immobilized on an anti-GST biosensor. Relative association rates (k_{ON}), dissociation rates (k_{OFF}), and dissociation constants (K_d) for nanodisc-tethered K-RAS4B binding to ARAF-RBD are shown in Fig. 4*D*. (*C*) Specific interaction of nanodisc-tethered WT K-RAS4B (GST-ARAF-RBD immobilized on tip, black) vs. nonspecific interaction of nanodisc-tethered WT and mutant K-RAS4B with the biosensor (GST-only immobilized on tip, colors), at the highest analyte concentration (35 μM nanodisc-conjugated K-RAS4B). Note that the nonspecific binding of WT and mutants exhibit identical signal amplitude and k_{ON} and k_{OFF} rates, indicating similar analyte concentrations. (*D*) Steady-state binding analyses of specific (GST-ARAF-RBD, black) and nonspecific (GST-only, red) interaction of nanodisc-conjugated K-RAS4B with the sensor tip in a steady-state analysis.

Table S1. PRE-induced broadening of the Ile Cδ probes of K-RAS4B

K-RAS4B: nanodisc	Parameter	Ile21	Ile24	Ile36	Ile46	Ile55	Ile84	Ile93	Ile100	Ile139	Ile142	Ile163
WT-GDP	I^o	0.58 ± 0.01	0.57 ± 0.01	1.47 ± 0.01	0.43 ± 0.01	0.53 ± 0.01	1.0 ± 0.01	0.46 ± 0.01	0.44 ± 0.01	0.34 ± 0.01	1.65 ± 0.01	0.23 ± 0.01
	I*	0.56 ± 0.01	0.46 ± 0.01	1.25 ± 0.01	0.29 ± 0.01	0.42 ± 0.01	1.0 ± 0.01	0.40 ± 0.01	0.30 ± 0.01	0.23 ± 0.01	1.01 ± 0.01	0.17 ± 0.01
	I^*/I^o	0.96 ± 0.02	0.81 ± 0.02	0.85 ± 0.01	0.67 ± 0.02	0.79 ± 0.02	1.0 ± 0.01	0.88 ± 0.02	0.69 ± 0.02	0.67 ± 0.03	0.61 ± 0.01	0.72 ± 0.04
WT	I^o	0.76 ± 0.01	0.35 ± 0.01	0.83 ± 0.01	0.47 ± 0.01	0.43 ± 0.01	1.0 ± 0.01	0.44 ± 0.01	0.22 ± 0.01	0.28 ± 0.01	1.6 ± 0.01	0.19 ± 0.01
	I*	0.68 ± 0.01	0.29 ± 0.01	0.54 ± 0.01	0.30 ± 0.01	0.34 ± 0.01	1.0 ± 0.01	0.41 ± 0.01	0.17 ± 0.01	0.21 ± 0.01	0.95 ± 0.01	0.14 ± 0.01
	I^*/I^o	0.89 ± 0.01	0.81 ± 0.02	0.65 ± 0.01	0.64 ± 0.01	0.80 ± 0.01	1.0 ± 0.01	0.93 ± 0.02	0.76 ± 0.03	0.75 ± 0.02	0.59 ± 0.01	0.72 ± 0.03
K5N	I^o	0.76 ± 0.01	0.43 ± 0.01	0.66 ± 0.01	0.52 ± 0.01	0.61 ± 0.01	1.0 ± 0.01	0.49 ± 0.01	0.23 ± 0.01	0.36 ± 0.01	1.57 ± 0.01	0.24 ± 0.01
	I*	0.72 ± 0.01	0.35 ± 0.01	0.50 ± 0.01	0.32 ± 0.01	0.49 ± 0.01	1.0 ± 0.01	0.44 ± 0.01	0.18 ± 0.01	0.25 ± 0.01	0.99 ± 0.01	0.15 ± 0.01
	I^*/I^o	0.94 ± 0.02	0.81 ± 0.03	0.76 ± 0.02	0.62 ± 0.02	0.79 ± 0.02	1.0 ± 0.01	0.91 ± 0.03	0.78 ± 0.05	0.69 ± 0.04	0.63 ± 0.01	0.63 ± 0.05
D153V	I^o	0.69 ± 0.01	0.30 ± 0.01	0.71 ± 0.01	OL	0.50 ± 0.01	1.0 ± 0.01	0.45 ± 0.01	OL	0.41 ± 0.01	1.57 ± 0.01	0.24 ± 0.01
	I*	0.68 ± 0.01	0.23 ± 0.01	0.60 ± 0.01	OL	0.42 ± 0.01	1.0 ± 0.01	0.44 ± 0.01	OL	0.27 ± 0.01	0.85 ± 0.01	0.16 ± 0.01
	I^*/I^o	0.98 ± 0.02	0.76 ± 0.05	0.83 ± 0.02	OL	0.84 ± 0.03	1.0 ± 0.02	0.96 ± 0.03	OL	0.66 ± 0.03	0.54 ± 0.01	0.67 ± 0.06
G12D	I^o	0.64 ± 0.01	0.30 ± 0.01	0.17 ± 0.02	0.50 ± 0.01	0.32 ± 0.01	1.0 ± 0.02	0.44 ± 0.01	0.13 ± 0.01	0.32 ± 0.02	1.40 ± 0.02	0.20 ± 0.02
	I*	0.67 ± 0.01	0.23 ± 0.01	0.16 ± 0.02	0.35 ± 0.01	0.27 ± 0.01	1.0 ± 0.01	0.38 ± 0.01	0.10 ± 0.01	0.19 ± 0.01	0.92 ± 0.01	0.10 ± 0.01
	I^*/I^o	1.05 ± 0.03	0.75 ± 0.05	0.91 ± 0.16	0.69 ± 0.03	0.82 ± 0.05	1.0 ± 0.02	0.84 ± 0.03	0.80 ± 0.12	0.59 ± 0.04	0.66 ± 0.01	0.52 ± 0.07
V29G	I^o	0.95 ± 0.01	0.55 ± 0.01	1.74 ± 0.01	0.49 ± 0.01	0.61 ± 0.01	1.0 ± 0.01	0.50 ± 0.01	0.39 ± 0.01	0.37 ± 0.01	1.61 ± 0.01	0.26 ± 0.01
	I*	0.95 ± 0.01	0.48 ± 0.01	1.32 ± 0.01	0.37 ± 0.01	0.51 ± 0.01	1.0 ± 0.01	0.44 ± 0.01	0.30 ± 0.01	0.25 ± 0.01	1.01 ± 0.01	0.20 ± 0.01
	I^*/I^o	0.99 ± 0.01	0.87 ± 0.02	0.75 ± 0.01	0.75 ± 0.02	0.82 ± 0.01	1.0 ± 0.01	0.88 ± 0.02	0.75 ± 0.02	0.68 ± 0.02	0.62 ± 0.01	0.74 ± 0.04
WT+ARAF	I^o	0.21 ± 0.03	0.49 ± 0.03	1.15 ± 0.03	0.36 ± 0.03	0.50 ± 0.03	1.0 ± 0.03	0.31 ± 0.03	0.33 ± 0.03	0.21 ± 0.03	2.67 ± 0.03	BBD
	I*	0.18 ± 0.02	0.42 ± 0.02	0.88 ± 0.02	0.30 ± 0.02	0.38 ± 0.02	1.0 ± 0.02	0.30 ± 0.02	0.25 ± 0.02	0.16 ± 0.02	1.53 ± 0.02	BBD
	I^*/I^o	0.86 ± 0.15	0.84 ± 0.06	0.76 ± 0.03	0.81 ± 0.08	0.75 ± 0.06	1.0 ± 0.03	0.95 ± 0.10	0.74 ± 0.09	0.74 ± 0.13	0.57 ± 0.01	BBD
WT+RALGDS	I^o	BBD	0.30 ± 0.03	0.47 ± 0.03	0.41 ± 0.02	0.62 ± 0.03	1.0 ± 0.02	0.31 ± 0.03	0.23 ± 0.03	0.23 ± 0.03	2.43 ± 0.02	BBD
	I*	BBD	0.30 ± 0.02	0.43 ± 0.02	0.32 ± 0.02	0.52 ± 0.01	1.0 ± 0.01	0.30 ± 0.02	0.23 ± 0.02	0.14 ± 0.02	1.29 ± 0.01	BBD
	I^*/I^o	BBD	1.0 ± 0.10	0.90 ± 0.07	0.76 ± 0.06	0.84 ± 0.04	1.0 ± 0.03	0.95 ± 0.10	1.0 ± 0.14	0.60 ± 0.11	0.53 ± 0.01	BBD

The data are presented as the peak intensities in the presence (I*) and absence (I^o) of Gd^{3+}-tagged lipids incorporated into the nanodiscs. The Gd^{3+}-induced broadening is shown as I^*/I^o ratio. Peak overlap (OL) and broadening beyond detection (BBD) in the absence of the PRE probe are indicated. Peak intensities and PRE ratios in each sample are normalized with respect to Ile84. Error is propagated based on spectral noise. K-RAS4B proteins were loaded with GMPPNP, except where indicated otherwise.

Table S2. Cluster statistics of the final HADDOCK solutions for the parallel (exposed) and semiperpendicular (occluded and semiexposed) orientations

Protein and orientation	Total cluster size	RMSD (Å)	Enb (kcal/mol)*	Eelec (kcal/mol)	Number of AIR violations	Buried surface area (Å^2)
K-RAS^{GDP}						
Exposed	128	3.1 ± 0.6	−903 ± 78.0	−804 ± 81.6	1.6 ± 0.5	3,555 ± 152.4
Occluded	66	5.5 ± 3.9	−570 ± 115	−503 ± 116	3.4 ± 2.1	2,488 ± 507.0
K-RAS^{GMPPNP}						
Exposed	63	3.4 ± 2.4	−823 ± 177	−743 ± 170	1.8 ± 0.9	3,088 ± 649.4
Occluded	89	3.1 ± 0.9	−820 ± 115	−741 ± 117	2.7 ± 1.3	3,105 ± 387.4
K-RAS^{GMPPNP}:ARAF-RBD						
Exposed	23	3.5 ± 2.3	−726 ± 194	−633 ± 180	2.5 ± 1.7	3,294 ± 550.4
Semiexposed	166	4.7 ± 1.7	−1,006 ± 108	−904 ± 107	4.2 ± 1.7	4,004 ± 409.9

Statistics are shown for the 10 lowest HADDOCK scored structures within each cluster. AIR, ambiguous interaction restraint.
*Enb (nonbonded energy) = Eelec (electrostatic energy) + Evdw (Van der Waals energy).

Table S3. PRE-induced broadening of the Ile Cδ probes of ARAF and RalGDS RBDs in complex with nanodisc-tethered K-RAS4B

	ARAF			RALGDS					
K-RAS: nanodisc	I54	I67	I76	αIle	βIle	γIle	δIle	εIle	ζIle
I^o	2.08 ± 0.01	1.0 ± 0.01	1.39 ± 0.01	0.82 ± 0.02	0.37 ± 0.02	2.78 ± 0.02	0.83 ± 0.02	1.46 ± 0.02	1.0 ± 0.02
I*	0.94 ± 0.01	1.0 ± 0.01	0.10 ± 0.01	0.76 ± 0.01	0.34 ± 0.01	2.20 ± 0.01	0.64 ± 0.01	1.02 ± 0.01	1.0 ± 0.01
I^*/I^o	0.44 ± 0.01	1.0 ± 0.01	0.08 ± 0.01	0.92 ± 0.03	0.91 ± 0.07	0.79 ± 0.01	0.77 ± 0.03	0.70 ± 0.01	1.0 ± 0.02

The isoleucines of RalGDS are indicated with Greek symbols as shown in Fig. S5. The peak intensities and PRE ratios are normalized with respect to Ile67 and ζIle for ARAF and RALGDS RBDs, respectively. I^o and I* are as described in Fig. 2*A*. Error is propagated based on spectral noise. K-RAS4B proteins were loaded with GMPPNP.